Materiales de Construcción 75 (359)
July-September 2025, e381
ISSN-L: 0465-2746
https://doi.org/10.3989/mc.2025.386724

Thermal insulation properties of pumice concrete: effect of porous aggregate containing coal gangue and fly ash

R. Feng[a], C. Yan[c], X. Wang[b] ✉, L. Jing[b], L. Yin[c], S. Liu[c], J. Zhang[b], W. Jing[b]

a. College of Science, Inner Mongolia University of Technology, (Hohhot, China)
b. School of Civil Engineering, Inner Mongolia University of Technology, (Hohhot, China)
c. School of Resources and Environmental Engineering, Inner Mongolia University of Technology, (Hohhot, China)
✉: wangxiaoxiao@imut.edu.cn

Received 7 May 2024
Accepted 10 January 2025
Available on line 6 February 2026

ABSTRACT: Coal gangue (CG) and fly ash (FA) were utilized to prepare CG-FA aggregate (CFA). The CFA concrete (CFAC) was produced by replacing natural pumice aggregate (NPA) with CFA. The optimal calcination parameters of CFA were obtained by orthogonal test with thermal conductivity (TC) as evaluation criterion. The TC, pore structure and micromorphology were tested to characterize thermal insulation properties. Results showed that the optimal calcination parameters for preparing CFA were a preheating temperature of 500 °C for 20 min and a calcination temperature of 1000°C for 10 min. The TC for CFAC decreases by 24.31% with 100% CFA. Filling pores with hydration products leads to a transition from macropores (>1 μm) to transition pores (0.01–0.1 μm) and capillary pores (0.1–1 μm), which complicates the heat transfer path and delays the heat transfer time.

KEY WORDS: Coal gangue; Fly ash; Natural pumice concrete; Thermal conductivity; Pore structure.

Citation/Citar como: Feng R, Yan C, Wang X, Jing L, Yin L, Liu S, Zhang J, Jing W. 2025. Thermal insulation properties of pumice concrete: Effect of porous aggregate containing coal gangue and fly ash. Mater. Construcc. 75(359):e381. https://doi.org/10.3989/mc.2025.386724

RESUMEN: *Propiedades de aislamiento térmico del hormigón con piedra pómez: efecto del árido poroso que contiene ganga de carbón y cenizas volantes.* Para la preparación del árido CG-FA (CFA) se utilizaron GGA de carbón (CG) y cenizas volantes (FA). El hormigón CFA (CFAC) se produjo sustituyendo el árido de piedra pómez natural (NPA) por CFA. Los parámetros óptimos de calcinación se obtuvieron mediante un ensayo ortogonal con la conductividad térmica como criterio de evaluación. La conductividad térmica, la estructura de los poros y la micromorfología se caracterizaron para evaluar las propiedades de aislamiento térmico. Los resultados mostraron que los parámetros de calcinación óptimos eran una temperatura de precalentamiento de 500°C durante 20min y una temperatura de calcinación de 1000°C durante 10min. La conductividad térmica disminuye un 24.31% con el 100% de CFA. El llenado de los poros con productos de hidratación conduce a una transición de macroporos (>1μm) a poros de transición (0.01-0.1μm) y poros capilares (0.1-1μm), lo que complica y retrasa el tiempo de transferencia de calor.

PALABRAS CLAVE: Ganga de carbón; Cenizas volantes; Hormigón de pumita natural; Conductividad térmica; Estructura de poros.

1. INTRODUCTION

The global production of concrete is estimated to be approximately 3.3 billion tons annually (1, 2). Aggregate accounts for more than 70% of concrete (3), which is derived from natural resources. In recent years, with the massive extraction of sand and gravel, the environment has been damaged which pose high environmental safety risks (4). Many countries have adopted restrictive policies for the exploitation of natural resources, resulting in a serious shortage of raw materials for concrete (5).

Lightweight aggregates, characterized by their light weight (6), excellent thermal insulation performance (7), and porous structure (8), have been extensively studied in recent years. Among these, natural pumice aggregate (NPA) is the most representative example. Natural pumice is formed from molten lava that solidifies with dense vesicles during volcanic eruptions (9), which can be served as an excellent porous aggregate after crushing to prepare natural pumice concrete (NPC). However, the NPAs are non-renewable resources. Moreover, the extraction and transportation processes result in significant energy consumption and environmental pollution. Clay has been extensively used for manufacturing artificial lightweight aggregates, due to its abundant SiO_2 and Al_2O_3 content (10). However, being a non-renewable resource, over-extraction of clay can result in resource depletion and significant harm to the soil's ecological environment (11).

Coal constitutes 74% of China's energy consumption, with the country producing nearly half of the global coal output (12). Coal gangue (CG), a major industrial solid waste, is produced during the processes of coal mining and washing (13, 14). It constitutes approximately 10% to 25% of emissions from raw coal (15) and is the most important source of pollution in mining areas. Fly ash (FA) is the final sediment of the coal burning process (16), with a global annual production of 8 billion tons (17). Large quantities of CG and FA occupy extensive land resources, and pose numerous environmental problems and significant ecological and safety hazards. Therefore, the selection of appropriate utilization technologies and processing methods to resourcefully utilize CG and FA is an important part of research.

In recent years, CG and FA have been investigated as cost-effective raw materials for aggregate production, showing significant potential in building material manufacturing. Studies have shown that SiO_2 and Al_2O_3 are the main components of CG and FA, which react at high temperatures to constitute skeleton structure of the aggregate (18). Researches focuse on the properties of aggregates prepared from sintered CG), fly ash FA, and other solid wastes, as well as the feasibility of using these sintered aggregates in the preparation of lightweight concrete (19, 20).

The effect of calcination temperature (21), pore forming agent content (22) on the water absorption, strength, and pore structure of sintered aggregate has been studied. Meanwhile, orthogonal tests (23), response surface methodology (24) were used to analyse the optimum preparation parameters for the preparation of aggregates to obtain sintered aggregates with excellent properties. High-strength ceramsite aggregate from FA and CaO with a compressive strength (CS) of 12.56 MPa (25). Porous aggregate was prepared using CG as raw material at a calcination temperature of 1100°C, with a cylinder CS of 4.5MPa, a water absorption rate of 12%, and an apparent density of 1800kg/m^3 (26). Lightweight aggregate was prepared using CG and sludge as raw materials, adding the clay and foaming agent with a sintering temperature of 1120°C, which has the cylinder CS of 6.1MPa, and the apparent density of 1220kg/m^3 (27). FA was utilized as the main raw material with clay added as an additive, sintering at a temperature of 1150°C to produce high-strength aggregate with a cylinder CS of 37.84MPa (28). The above studies show that aggregates with excellent performance can be prepared by using CG and FA as primary raw materials. Furthermore, researchers have incorporated aggregates into concrete production and discovered that solid waste aggregate concrete offers benefits such as light weight (29), extended service life (30), and enhanced thermal insulation and fire resistance (31). A literature review (19) indicates that concrete made with sintered fly ash achieves densities from 1600 and 2000 kg/m^3 and CS ranging from 22 to 43 MPa. Concrete incorporating FA aggregate demonstrates promising performance in structural applications. Additionally, numerous studies have explored the utilization of solid waste to produce lightweight aggregate. These aggregates can be incorporated into concrete to reduce the self-weight and enhance the thermal insulation properties (32, 33).

The feasibility of utilizing CG and FA to prepare porous insulating aggregates was studied, and the optimal calcination parameters for the preparation of the aggregates were proposed. Porous aggregates were incorporated into NPC to examine their impact on its insulation performance, offering theoretical insights for the application of solid waste aggregates in thermal insulation building materials. Furthermore, we analyzed the environmental impact and costs associated with the production and use of solid waste aggregate concrete, ensuring its application offers substantial environmental benefits.

2. MATERIALS AND METHODS

2.1. Preparation of CFA

2.1.1. Raw materials

The raw materials for preparing CFA are CG and FA. The chemical compositions and main phase of CG and FA are shown in Table 1 and Figure 1. The SiO_2 and Al_2O_3 are the main chemical compositions of CG and FA. The main crystalline phases of CG are anorthite, kaolinite and quartz. In Figure 2 is illustrated the particle size distribution of CG and FA. The median particle sizes (D50) were determined to be 17.825 µm for CG and 12.057 µm for FA, respectively.

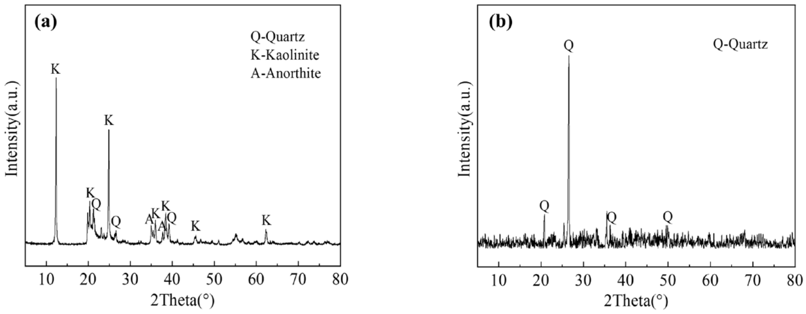

Figure 1. XRD pattern of CG and FA.

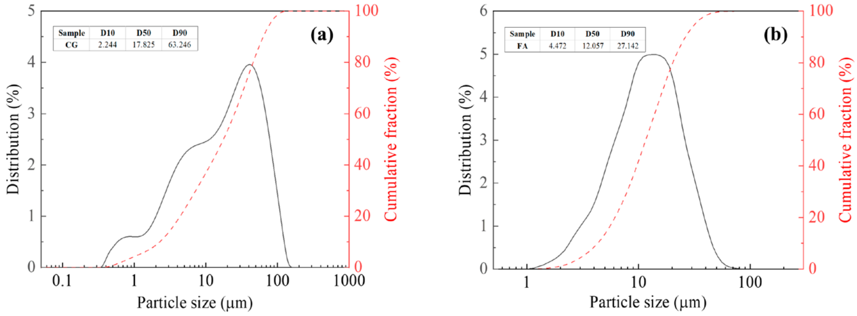

Figure 2. Particle size distribution of CG (a) and FA (b).

Table 1. Chemical composition (wt%).

Material	Chemical composition								
	SiO_2	Al_2O_3	CaO	Fe_2O_3	MgO	K_2O	Na_2O	TiO_2	Others
CG	51.20	46.90	0.20	0.57	0.04	0.09	0.03	0.71	0.26
FA	48.08	22.69	15.17	4.45	2.77	1.53	2.01	0.61	2.69

2.1.2. Preparation of CFA

In Figure 3 is shown the process of CFA production. CG was initially crushed and then ground into a powder using a ball mill. Subsequently, the powder was sieved through a 125 µm screen. The sieved CG and FA were then mixed uniformly in a mass ratio of 8:2. They were placed into the granulator for granulation. Water was sprayed to make the raw materials roll into pellets in the granulator. In the granulation process, the water should be evenly sprayed. Water constitutes approximately 25% of the total mass of raw materials. The raw material pellets, with particle sizes ranging from 9.5 to 16 mm, were sieved and then dried in an oven for 2 hours at 105°C. The raw material pellets were removed and placed in the high-temperature furnace for calcination according to set temperature. The CFA was taken out immediately after calcination and cooled at room temperature to produce CFA. This study employs an orthogonal experimental design, a multifactorial and multilevel research method that efficiently identifies optimal combinations while saving time (34-36).

The performance of CFA is affected by the parameters A (preheating temperature), B (preheating time), C (calcination temperature) and D (calcination time). The factors and levels of the orthogonal experiment are detailed in Table 2.

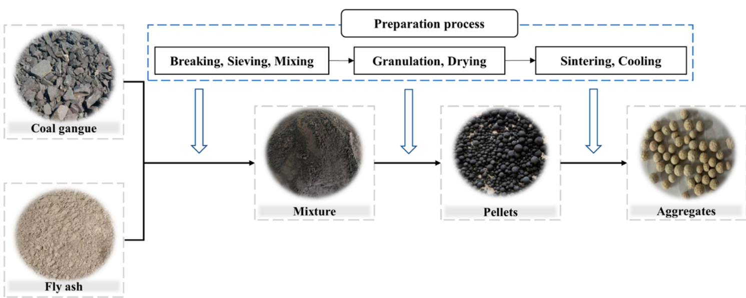

Figure 3. Preparation process.

Table 2. Factors and levels of orthogonal experimental.

Levels	Factors			
	A/ºC	B/min	C/ºC	D/min
1	400	10	1000	10
2	500	20	1100	20
3	600	30	1200	30

A and B represent preheating temperature and preheating time, respectively. C and D represent calcination temperature and calcination time, respectively.

2.2. Preparation of CFAC

2.2.1. Raw materials

The P·O 42.5 ordinary silicate cement was used. In Table 3 and Table 4 are indicated the physical properties and chemical composition of the cement, respectively. The coarse aggregates used in the test included NPA and the prepared CFA. In Table 5 is shown the main chemical composition of NPA. In Figure 4 is shown the mineralogical composition of NPA, primarily comprising albite, calcite, kaolinite, and anorthite. The sand was selected as natural river sand with a bulk density of 1461 kg/m³, an apparent density of 2550 kg/m³, and a fineness modulus of 2.9. The water reducing agent has a water reduction rate of 20%. Fresh water was used.

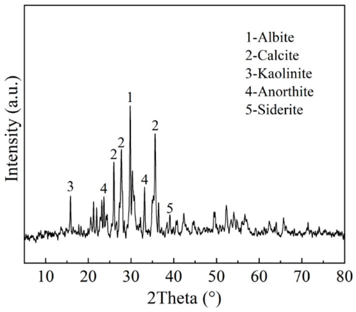

Figure 4. XRD pattern of cement.

Table 3. Physical properties of cement.

Initial setting time (min)	Final setting time (min)	Fineness (%)	Water requirement of normal consistency (g)	CS (MPa)	
				3d	28d
125	255	1.92	155	22.8	44.7

Table 4. Chemical composition of cement.

CaO	SiO_2	Al_2O_3	Fe_2O_3	MgO	Na_2O	Others
63.33	23.03	5.11	3.34	2.06	0.70	2.43

Table 5. Chemical composition of NPA (wt%).

SiO_2	Al_2O_3	Fe_2O_3	CaO	MgO	Na_2O	Others
45.62	15.26	10.46	8.37	6.96	5.24	7.63

2.2.2. Mix proportion

The NPC with the strength class of LC30 was prepared according to the Chinese Specification JGJ55-2011 and JGJ51-2002. On the basis of baseline mix ratio, the rest of the components remained unchanged, and the prepared CFA was utilized to replace the NPA in NPC. In this study, the prepared CFA and NPC were pre-soaked in water to ensure complete saturation. After soaking, any excess water was drained from the aggregates prior to concrete preparation. This approach can resolve water deficiency caused by the water absorption of the aggregates. This step is essential to guarantee the performance and quality of the concrete. In particular, the volumetric substitution method was used, and substitution rates were 0%, 25%, 50%, 75%, and 100%. In Table 6 is shown the mix ratios of CFAC.

2.3. Characterization methods

The physical properties of CFA, including cylinder compressive strength (CCS), water absorption rate, apparent density and packing density were determined in accordance with the Chinese Specification GBT17431.2-2010. The CS of CFAC was tested in compliance with the Chinese Specification GB/T50081-2019. The TC of CFAC was examined using a DRE-III thermal conductivity tester. The pore structure of CFAC was examined using a nuclear magnetic resonance meter (MesoMR-60S type). A nuclear magnetic resonance meter (MesoMR-60S type) was used to characterize the pore structure of CFAC. A scanning electron microscope (FEI QUANTA 650 FEG type) was used for the microscopic tests.

Table 6. Mix proportions.

Specimens	Ceramsite (kg)	NPA (kg)	Cement (kg)	Water (kg)	Fly ash (kg)	Sand (kg)	Water reducer (kg)	28d CS (MPa)
LC30-0	0	562	352	144	80	739	3.024	35.8
LC30-25	160	421	352	144	80	739	3.024	32.9
LC30-50	320	281	352	144	80	739	3.024	29.3
LC30-75	480	140	352	144	80	739	3.024	28
LC30-100	639	0	352	144	80	739	3.024	27.4

3. RESULTS AND DISCUSSION

3.1. Characterization of CFA

3.1.1. Analysis of orthogonal test results

The calcination procedure of CFA was determined based on orthogonal tests with TC as the evaluation criterion. The orthogonal test results are shown in Table 7. It is observed that the TC of CFA ranges from 0.1559 to 0.2408 W/(m·K). The TC of CFA ranges 0.1559 to 0.2408 W/(m·K). In Table 8 is shown the range analysis of TC. Kn (n=1,2,3) represents the average TC of CFA under varying factor contents. The R value, which is defined as the difference between Kmax and Kmin for each factor, is employed to evaluate the influence degree of each factor exerts on the thermal conductivity (TC) of CFA (37, 38). The R value from the largest to the smallest are calcination temperature, preheating temperature, preheating time, and calcination time, indicating that the calcination temperature has the greatest effect on CFA's TC. With the TC used as the evaluation criterion, the optimal calcination parameters were determined to be preheating time of 20 minutes, preheating temperature of 500 °C, calcination time of 10 minutes, and calcination temperature of 1000 °C.

3.1.2. Physical properties of CFA

CFA was prepared using the optimal calcination parameters. In Table 9 is shown the physical properties of the prepared CFA and NPA. The CFA exhibits a TC of 0.1416 W/(m·K) and a CCS of 2.5 MPa. In comparison, the TC and CCS of NPA are 0.2424 W/(m·K) and 1.18 MPa, respectively. Therefore, compared with NPA, the CFA prepared in this study increases the CCS by 52.8% and reduces the TC by 41.6%. The thermal insulation performance and mechanical properties of CFA are superior to NPA. Therefore, CFA can be used to replace NPA in concrete preparation.

Table 7. L9(34) orthogonal experimental design and properties of CFA.

No.	Factors				Results
	A/ºC	B/min	C/ºC	D/min	TC (W/(m·K))
1	400	10	1000	10	0.1703
2	400	20	1200	20	0.2046
3	400	30	1100	30	0.1909
4	500	10	1200	30	0.2207
5	500	20	1100	10	0.1604
6	500	30	1000	20	0.1559
7	600	10	1100	20	0.2331
8	600	20	1000	30	0.1884
9	600	30	1200	10	0.2408

Table 8. Range analysis calculation of orthogonal test.

/	A/ºC	B/min	C/ºC	D/min
K_1	0.189	0.208	0.172	0.191
K_2	0.179	0.184	0.195	0.198
K_3	0.221	0.196	0.222	0.200
R	0.042	0.024	0.050	0.009

k represents the mean value; *R* represents the range.

Table 9. Physical properties of CFA and NPA.

Types of aggregates	Apparent density (Kg/m^3)	Packing density (Kg/m^3)	Water absorption rate (%)	CCS (MPa)	TC (W/(m·K))
CFA	1745	858.76	24.3	2.5	0.1416
NPA	1690	810	9.04	1.18	0.2424

3.2. Characterization of CFAC

3.2.1. Compressive strength and thermal conductivity

In Figure 5 is shown the effect of CFA content on the TC and the CS of CFAC. The CS of NPC decreases with the substitution rate of CFA increases. Previous studies (39, 40) have established that the replacement of natural aggregates with artificial aggregates reduces concrete strength directly proportional to the quantity of artificial aggregates used. The findings of this study are consistent with these results. Due to the minor enamel layer produced on the surface during sintering (11), CFA has a smoother surface than NPA. Consequently, the bond between CFA and the cement paste is weaker than that of NPA, resulting in diminished mechanical performance of CFAC. However, CCS of CFA surpasses that of NPA, suggesting that the incorporation of CFA does not significantly reduce the strength of NPC.

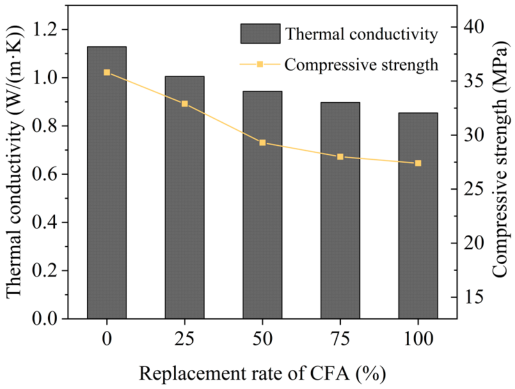

Figure 5. The effect of CFA's replacement rate on the compressive strength and thermal conductivity.

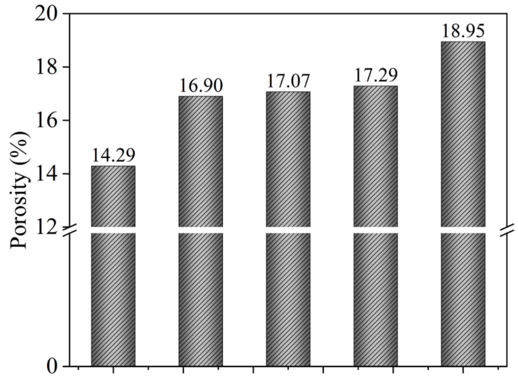

Figure 6. The effect of replacement rate of CFA on porosity.

TC is a significant parameter to measure concrete's thermal insulation property. The TC decreases as the CFA substitution rate increases, as shown in Figure 5. The TC of CFAC is 0.85 to 1.13 W/(m·K), significantly lower than that of ordinary concrete (1.65 W/(m·K)) (41). The TC of CFAC decreases by 24.31% when the substitution rate increases from 0% to 100%. The TC for NPA and CFA is 0.2424 and 0.1416 W/(m·K), indicating that the thermal performance of CFA is better than that of NPA. Therefore, substituting NPA with CFA enhances the thermal performance of concrete.

3.2.2. Pore structure

In Figure 6 is shown the influence of CFA replacement rate on the porosity of CFAC. As the CFA replacement rate increases, the porosity of the CFAC increases. The porosity of CFAC increased by 24% when the substitution rate of CFA increased from 0% to 100%. The porosity of CFA and NPA were measured to be 34.29% and 27.94%. Therefore, replacing NPA with CFA can increase the number of internal pores in CFAC. Additionally, during the preparation of CFA, the surface of calcined CFA becomes covered with numerous crystalline phases, forming a smooth enamel layer (42), while the surface of NPA has a rough porous structure (shown in Figure 7). Consequently, the bond strength between CFA and cement paste in concrete is weaker compared to NPA, leading to the formation of pores in the interfacial transition zone due to insufficient bonding (43). The TC of CFAC is closely linked to its porosity, with higher porosity corresponding to lower TC (44). In Figure 8 is presented a correlation analysis between the porosity and TC of CFAC, revealing a negative correlation with a coefficient of 0.91. The increase of porosity leads to the improvement of insulation performance of concrete, which is consistent with Dai's (45) and Hao's (46) findings.

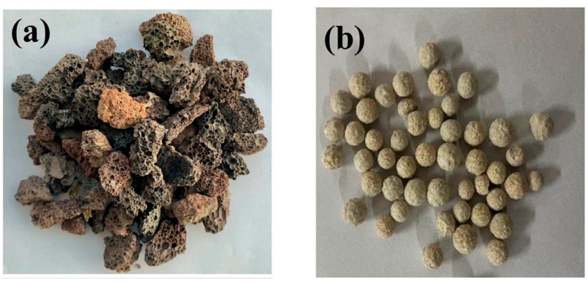

Figure 7. Apparent appearance. (a) NPA; (b) CFA.

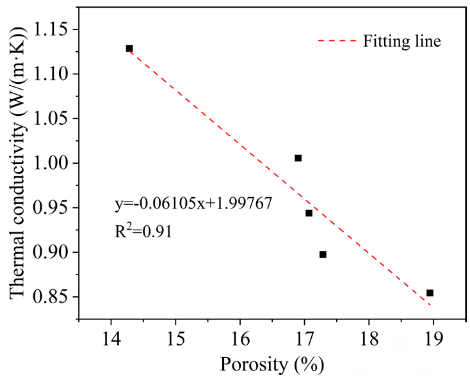

Figure 8. Correlation between porosity and thermal

In Figure 9(a) is shown the pore size distribution of CFAC under different CFA replacement rates which is shown a "four-peak" structure. Moreover, the pore size of CFAC is distributed in the interval of 0.002–200 µm. The proportion in volume of "peak 1" and "peak 2" gradually increases with the increase in CFA substitution rate, whereas the volume ratio of "peak 3" and "peak 4" gradually decreases. In addition, the corresponding pore size of "peak 2" decreases from 0.2 µm to 0.08 µm with the increase in substitution rate.

The pores of CFAC are categorized into four classes: gel pores (<0.01 μm), transition pores (0.01–0.1 μm), capillary pores (0.1–1 μm), and large pores (>1 μm) (47). As shown in Figure 9(b), the percentage of large pores decreases from 41.19% to 6.52%, the percentage of capillary pores increases from 13.13% to 24.9%, and the percentage of transition pores increases from 24.88% to 45.82% when the CFA substitution rate increases from 0% to 100%. The finding indicates that the large pores are shifted to transition and capillary pores. According to the pore size distribution curves of CFA and NPA in Figure 9(c), CFA exhibits a "bimodal" structure, with pore sizes primarily concentrated between 1 μm and 10 μm, while NPA shows a "multimodal" structure and the pore size is concentrated in 30 μm-350 μm, which also proves that CFA can refine the pore structure of NPC, which is consistent with the findings of Wang et al. (44). The restricted movement of gas molecules within the pore structure reduces convective heat transfer, ultimately decreasing the TC of CFAC (48). Additionally, cement paste can penetrate the interior of CFA through the surface pores, decreasing the pore diameter and increasing the number of pores. This results in an increase in the surface area of the pore walls during heat transfer, thus lengthening the heat conduction distance and delaying heat transfer (49), which enhances the thermal insulation properties of CFAC.

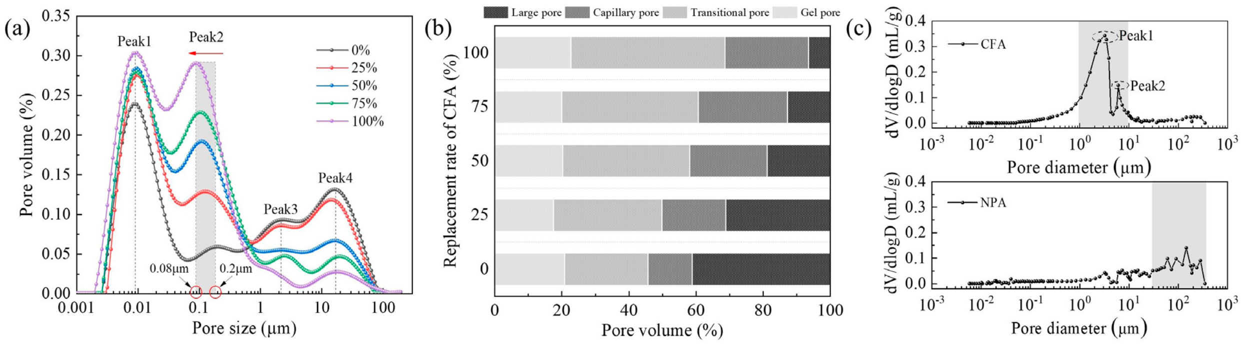

Figure 9. Pore structure. (a) Pore size distribution of CFAC; (b) Pore size volume fraction; (c) Pore size distribution of CFA and NPA.

In Figure 10 is shown the SEM images of NPC and CFAC with a 50% CFA replacement rate. The internal pore and crystal structures of NPC and CFAC can be observed. The pore structure of CFA is more complex than that of NPA, and there are pores of different sizes and uneven distribution in CFA, which are formed by gases released during the oxidation reaction during sintering (43). In Figure 11 is shown the XRD pattern and EDS diagram of CFA in region 1. The main constituent elements of the crystals are Ca, Si, Al and O. Therefore, main crystal composition of CFA is anorthite ($CaAl_2Si_2O_8$). It is found that anorthite can not only form the skeletal structure of the CFA, but it is also a good thermal insulation material (50), which has a contributing effect on improving the thermal insulation performance of NPC. Additionally, fibrous hydrated calcium silicate (C-S-H) crystals were found in the internal pores of CFA. The reason is that the CFA has the property of "water absorption", and CFA absorbs the water in the cement paste during the concrete curing process. When there is a moisture difference between CFA and cement paste, the cement paste enters the internal pores of CFA, resulting in the formation of C-S-H in the pores of CFA. C-S-H partially fills the pores, which is highly resistant to the process of heat penetration by air (51-53), which explains the improvement in thermal insulation performance of CFA compared to NPC.

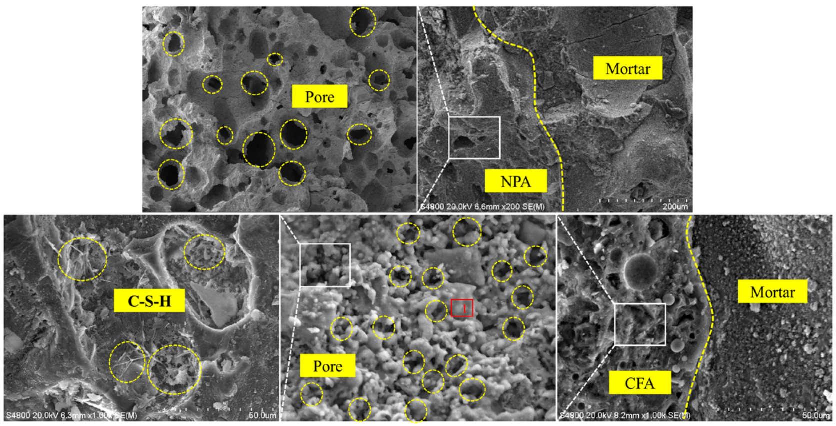

Figure 10. SEM images. (a) NPC; (b) CFAC.

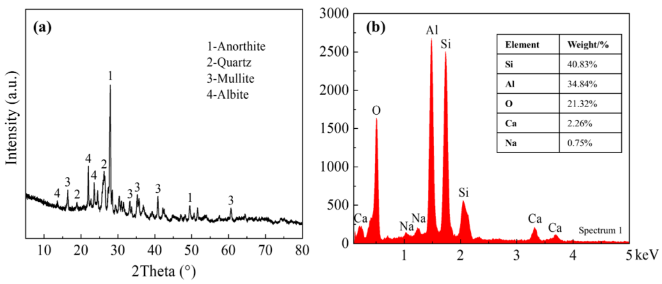

FIGURE 11. XRD pattern (a) and EDS diagram (b) of CFA in region 1.

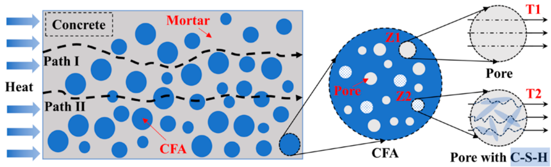

FIGURE 12. Thermal insulation mechanism diagram based on multi-scale.

A schematic diagram of the thermal insulation mechanism of CFAC is shown in Figure 12. Macroscopically, the heat transfer mode of CFAC includes two paths: (1) heat conduction through the cement paste (Path I) and (2) heat conduction through the cement paste and CFA (Path II). The SEM results show that the distribution of CFA pores inside the concrete is more than that in the cement paste. Moreover, the size of CFA pores is larger than that of the cement paste. Thus, the heat transmission through Path II significantly affects the enhancement of concrete's thermal insulation performance. Given the porous structure of CFA, the heat conduction in the aggregate is mainly between the gas and the solid phase. The conduction velocity of heat in the gas phase is lower than that in the solid (54). Thus, CFA has a good thermal insulation effect. The microscopic observation of CFA's pore structure indicates that the pore structure in CFA is divided into two categories (Z1 and Z2 in Figure 12). Z1 indicates that the heat is conducted in the ordinary pores, and the conduction time is T1. Z2 indicates the pore structure filled by C-S-H. The heat conduction path in Z2 becomes complicated, leading to the prolongation of heat transfer time (T2 > T1) (55). Thus, the thermal insulation performance of NPC is enhanced.

4. THERMAL CONDUCTIVITY CALCULATION MODEL

4.1. Modeling of thermal conductivity prediction

Multiscale analysis is an important tool for studying nonhomogeneous materials. CFAC is a typical composite material. This study used the multiscale division of cementitious materials by Constantinides (56) and divided concrete into four scales, as shown in Figure 13. The scales are as follows:

(1) Scale I is a 10^{-8}–10^{-4} m scale, which mainly consists of nanoscale particles. It is considered a C-S-H gel, originating from the hydration of C_2S and C_3S in cement-based composites.
(2) Scale II is a 10^{-6}–10^{-4} m scale, which is considered a cement paste. It contains C-S-H gel, large-scale C-H crystals, unhydrated cement clinker particles, and other material phases.
(3) Scale III is a 10^{-3}–10^{-2}m scale, which is a mortar. It consists of cement paste and fine aggregate.
(4) Scale IV is a 10^{-2}–10^{-1} scale, which is concrete. It consists of a mortar matrix and coarse aggregate.

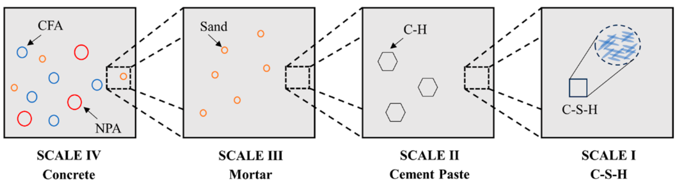

FIGURE 13. A four-scale model.

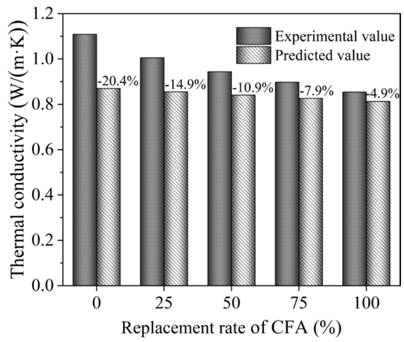

FIGURE 14. Comparison of predicted and experimental values.

The TC of CFAC was predicted using the Maxwell model, shown in Equation 1. The Maxwell model operates under the assumption that the dispersed phases do not interact with one another and are uniformly dispersed in the matrix (57).

$$\frac{K-k_m}{K+2k_m}=\sum_{i=1}^{N}v_i\left[\frac{k_i-k_m}{k_i+2k_m}\right] \quad [1]$$

where K represents the TC of the composite, N represents the count of dispersed phases, v_i represents the volume fraction of the ith phase, k_i represents the TC of the ith phase, and k_m represents the TC of the continuous phase.

4.2. Calculation of thermal conductivity

According to the multiscale division of CFAC, the calculation of TC was conducted from Scale I–Scale IV using the above equations. Scale I–Scale II can be regarded as the hydration process of the cement paste. The TC of C_3S, C_2S, C-H and C-S-H as 3.35, 3.45, 1.32 and 0.98 W/(m·K) was calculated (58), by using the molecular dynamics simulation method. According to the determination of C_3A, C_4AF, AFm, and Aft by Du et al (59), the TC values are 3.74, 3.17, 2.56, and 2.19 W/(m·K). The VCCTL model constructs the cementite structure based on the particle size distribution of real cement particles and spatial distribution of mineral phases. The model also controls the cement hydration based on the kinetic principle of chemical reaction, which can simulate the cement hydration process well (60, 61). The volume fraction for each phase can be obtained by simulating cement paste's hydration process through VCCTL model (Table 10). The TC of the cement paste can be determined by taking volume fraction and TC into Equation (1).

Table 10. Volume fraction (%).

Pore	C_3S	C_2S	C_3A	C_4AF	CSH	CH	AFt	AFm
19.75	5.47	4.14	0.42	4.75	40.66	14.85	6.71	3.25

The TC of cement mortar in Scale III is derived from a composite of cement paste and sand. In Scale IV, the TC of CFAC is obtained by integrating the dispersed and continuous phases, where cement mortar serves as the continuous phase and CFA and NPA function as the dispersed phases. In Figure 14 is presented the results of CFAC TC obtained through this method. The predicted TC values are consistently lower than the actual measurements. This discrepancy arises because the calculations do not account for the thermal resistance at the boundaries between the coarse aggregate and cement mortar, as well as between the cement paste and sand. The error range between the actual values and predicted values of CFAC spans from 5% to 20%. The Maxwell model can be used to predict the TC of CFAC.

5. CARBON EMISSIONS AND ECONOMIC ANALYSIS

5.1. Carbon emissions

The total carbon emissions per unit volume of concrete is a crucial indicator for assessing environmental impact. Total CO_2 are equal to the sum of the CO_2 produced in the various processes used to produce concrete. The CO_2 Emission was calculated according to Equations [2], [3] and [4]:

$$E_1=\sum W_k \times G_k \quad [2]$$

Where E_1 represents the total CO_2 emissions from the raw material extraction unit, W_k represents the mass of the k-th raw material, kg/t, and G_k represents the carbon emission factor for extracting the k-th raw material, $kgCO_2$/kg.

$$E_2=\sum W_k \times S_k \times G_k \quad [3]$$

Where E_2 represents the total CO_2 emissions from the transportation unit, W_k denotes the mass of the k-th raw material requiring transportation, kg, S_k is the distance needed to transport the k-th raw material, km, and G_k is the carbon emission factor for diesel transportation of raw materials, $kgCO_2$(/kg·km).

$$E_3=\sum E_P \times G_P \quad [4]$$

Where E_3 is the total CO_2 emissions from the production unit, E_P represents the electricity consumption during the concrete production process, kW·h/t, G_P represents the carbon emission factor of electricity, $kgCO_2$/(kW·h).

5.1.1. E_1 calculation

Based on the Chinese Specification GB/T 51 366–2019 and relevant literature research, the CO_2 emissions from the raw material extraction unit were calculated. In Table 11 is shown the production list of CFAC. Therefore, the carbon emission (G1) of CFAC during its production (treatment) is: 352×0.732+207.8×0.0345+511.2×0.079+3.024×0.00251 +739×0.12+144×0.000148=309.27kg CO_2/t.

Table 11. Volume fraction (%).

Classification	Resource	Use level	Emission factor (kg CO_2/kg)
Resource consumption	CG (kg)	511	0.079000 (62)
	FA (kg)	208	0.034500 (63)
	Cement (kg)	352	0.732000 (63)
	Sand (kg)	739	0.002510 (64)
	Water reducer (kg)	3	0.720000 (63)
Energy consumption	Water (kg)	144	0.000148 (63)
	Electric power (kW·h)	97	0.940200 (63)

5.1.2. E_2 calculation

Cement, CG, FA, and sand used in the raw materials for CFAC were transported to the factory by 30 diesel vehicles, covering distances of 95, 38, 100, and 35 km. The carbon emission factor for a 30t diesel vehicle is 0.078 kg CO_2/(t·km) in accordance with the Chinese specification GB/T 51366–2019. Thus, the carbon emission from the transportation unit is: $352×0.078×95×10^{-3} + 511.2×0.078×38×10^{-3} + 207.8×0.078×100×10^{-3} + 739×0.078×35×10^{-3} = 7.76$ kg CO_2/t.

5.1.3. E3 calculation

The consumption of electricity is approximately 97.188 (kW·h)/t. The carbon emission factor of electricity in China is approximately 0.9402 kg CO_2/kW·h, according to the literature. Consequently, 97.188 × 0.9402 = 91.38 kg CO_2/t is the carbon emission from the electricity used in the production of CFAC. The total carbon emission of CFAC is 309.27 + 7.76 + 91.38 = 408.41 kg CO_2/t on the basis of life cycle assessment (LCA).

5.2. Economic analysis

The economic analysis of CFAC was evaluated by the cost of producing per unit volume of concrete, which is shown in Table 12. The cost of resource consumption is 51.584 USD/m^3, the cost of energy consumption is 11.719 USD/m^3, total cost of CFAC production is 63.303 USD/m^3.

Table 12. Cost indices of raw materials.

Classification	Resource	Use level	Unit cost (USD/t)	Cost (USD)
Resource consumption	CG (kg)	511	5.60 (65)	2.862
	FA (kg)	208	13.00 (65)	2.701
	Cement (kg)	352	98.00 (65)	34.496
	Sand (kg)	739	14.00 (65)	10.346
	Water reducer (kg)	3	390.00 (65)	1.179
Energy consumption	Water (kg)	144	0.39 (65)	0.056
	Electric. power (kW·h)	97	0.12 (62)	11.663

Table 13. Cost comparison and carbon emissions of different concrete types.

Source	Concrete type	CO_2 Emission (kg CO_2/kg)	Cost (USD/m^3)
This study	CFAC	408	63.3
Yu et al. (2017) (66)	Ordinary aggregate concrete	450	75.5
Liu et al. (2022) (67)	Artificial light-weight aggregate concrete	498	82.7

5.3. Carbon emissions and cost comparison of different concrete types

Compared with ordinary aggregate concrete and artificial lightweight aggregate concrete, the CFAC produced in this study had lower economic costs and lower carbon emissions, as shown in Table 13.

6. CONCLUSIONS

CG and FA were used to produce porous insulating aggregates. Utilizing solid waste to prepare aggregates is an essential method for achieving comprehensive utilization of solid waste, effectively addressing the disposal issues of solid waste while preventing resource waste and environmental damage caused by excessive exploitation of natural aggregate resources. Concrete, the most commonly used building material, requires enhanced thermal insulation performance to reduce building energy consumption. This study evaluates the impact of incorporating solid waste porous aggregates into concrete to improve its insulation performance. These aggregates present a low-carbon, eco-friendly alternative for new building materials with significant application potential. The main conclusions obtained in this study are as follows:

(1) The optimum sintering procedure for the preparation of coarse aggregate using CG and FA is as follows: preheating phase at 500 °C for 20 min, followed by a calcination phase at 1000 °C for 10 min. The CFA prepared based on the optimal calcination procedure has a porous structure, CCS of up to 2.5MPa, and the TC of 0.1416 W/(m·K).

(2) The aperture distribution curve of CFAC presents a “four-peak” structure. When the CFA replacement rate increases from 0% to 100%, the proportion of large pores decreases by 84.17%, whereas the proportions of capillary pores and transition pores increase by 47.27% and 45.7%, respectively. Moreover, the proportion of gel pores does not change.

(3) The C-S-H fills the CFA’s internal pores, which restricts the movement of gas molecules within the pores and significantly reducing the heat penetration capability of air. The conduction path of heat in CFA becomes complicated, and the heat transfer time is prolonged, thereby improving the thermal insulation performance of NPC.

(4) The Maxwell model can predict the TC of CFAC based on the multiscale approach with a prediction accuracy of 5%–20%.

(5) The total carbon emission of the CFAC is 408.41kg CO_2/t and the total cost of CFAC production is 63.303 USD/m^3.

Acknowledgements

This study was supported by the National Natural Science Foundation of China (Grant No.52469023), the Basic Scientific Research Expenses Program of Universities Directly under Inner Mongolia Autonomous Region (Grant No. JY20240076, JY20220179), the Central Guidance on Local Science and Technology Development Fund (Grant No. 2022ZY0160, 2021ZY0024), the Ordos City Key R&D Project (YF20232358), and the Science and Technology Project of Inner Mongolia (Grant No. 2023YFDZ0049, 2022YFDZ0023, 2021GG0317, 2022YFHH0153).

Authorship contribution statement

Rongrong Feng: Write-up - review & editing, Write-up - original draft.
Xiaoxiao Wang: Write-up - review & editing, Fund raising.
Changwang Yan: Conceptualization, Resources, Fund raising.
Lei Jing: Supervision, Fund raising.
Liqiang Yin: Supervision.
Shuguang Liu: Resources, Fund raising.
Ju Zhang: Visualization.
Weize Jing: Visualization, Research.

Declaration of competing interest

The authors of this article declare that they have no financial, professional or personal conflicts of in-ter-est that could have inappropriately influenced this work.

REFERENCES

1. Tanyıldızı M, Gökalp İ. 2023. Utilization of pumice as aggregate in the concrete:A state of art. Constr. Build. Mater. 377:131102. https://doi.org/10.1016/j.conbuildmat.2023.131102

2. Ikponmwosa E, Ehikhuenmen S. 2017. The effect of ceramic waste as coarse aggregate on strength properties of concrete. Niger. J. Technol. 36(3):691-696. https://doi.org/10.4314/njt.v36i3.5
3. Bendixen M, Best J, Hackney C, Iversen L. 2019. Time is running out for sand. Nature. 7763(571):29-31. https://doi.org/10.1038/d41586-019-02042-4.
4. Shang XY, Chang JL, Yang JW, Ke XJ, Duan ZH. 2022. Life cycle sustainable assessment of natural vs artificial lightweight aggregates. J. Clean. Prod. 367:133064. https://doi.org/10.1016/j.jclepro.2022.133064.
5. Feng W, Tang Y, Yang Y, Cheng Y, Qiu JH, Zhang HX. 2023. Mechanical behavior and constitutive model of sustainable concrete:seawater and sea-sand recycled aggregate concrete. Constr. Build. Mater. 364:130010. https://doi.org/10.1016/j.conbuildmat.2022.130010.
6. Zeng YS, Li XM, Tang AP, Zhao N, Li L, Jia SM. 2023. Axial compressive behavior of basalt and polyacrylonitrile fibers reinforced lightweight aggregate concrete with industrial waste ceramsite-Lytag after freeze-thaw cycles. J. Build. Eng. 76:107402. https://doi.org/10.1016/j.jobe.2023.107402.
7. Petrillo A, Colangelo F, Farina I, Travaglioni M, Salzano C, Cioffi R. 2022. Multi-criteria analysis for Life Cycle Assessment and Life Cycle Costing of lightweight artificial aggregates from industrial waste by double-step cold bonding palletization. J. Clean. Prod. 351:131395. https://doi.org/10.1016/j.jclepro.2022.131395.
8. Bian ZW, Huang YJ, Lu JX, Ou GF, Yang SQ, Poon CS. 2023. Development of self-foaming cold-bonded lightweight aggregates from waste glass powder and incineration bottom ash for lightweight concrete. J. Clean. Prod. 428:139424. https://doi.org/10.1016/j.jclepro.2023.139424.
9. Rashad AM. 2019. A short manual on natural pumice as a lightweight aggregate. J. Build. Eng. 25:100802. https://doi.org/10.1016/j.jobe.2019.100802.
10. Geng J, Niu SL, Han KH, Wang YZ, Zhu J, Yang ZH, Liu JS, Zhang HJ, Sun XB, Liang B, Zheng Y. 2024. Properties of artificial lightweight aggregates prepared from coal and biomass co-fired fly ashes and sewage sludge fly ash. Ceram. Int. 50(16):28609-28618. https://doi.org/10.1016/j.ceramint.2024.05.172.
11. Jia G, Wang Y, Yang F, Ma Z, Li B, Zhang L. 2023. Preparation of CFB fly ash/sewage sludge ceramsite and the morphological transformation and release properties of sulfur. Constr. Build. Mater. 373:130864. https://doi.org/10.1016/j.conbuildmat.2023.130864.
12. Zhang Y, Ling TC. 2020. Reactivity activation of waste coal gangue and its impact on the properties of cement-based materials-A review. Constr. Build. Mater. 234:117424. https://doi.org/10.1016/j.conbuildmat.2019.117424.
13. Zhang L, He C, Yang A, Yang Q, Han JS. 2018. Modeling and implication of coal physical input-output table in China-based on clean coal concept. Resour. Conserv. Recycl. 129:355-365. https://doi.org/10.1016/j.resconrec.2016.10.005.
14. Chao L, Xing YM, Hou XH. 2024. Optimization of properties of aeolian sand cement-based materials by metakaolin. J. Inner. Mongolia. Univ. Technol. Nat. Sci. Ed. 03:278-283. https://doi.org/10.13785/j.cnki.nmggydxxbzrkxb.2024.03.014.
15. Huang GD, Ji YS, Li J, Hou ZH, Dong ZH. 2018. Improving strength of calcinated coal gangue geopolymer mortars via increasing calcium content. Constr. Build. Mater. 166:760-768. https://doi.org/10.1016/j.conbuildmat.2018.02.005.
16. Gómez Casero MA, Dios Arana CD, Bueno Rodríguez JS, Pérez Villarejo L, Eliche Quesada D. 2022. Physical, mechanical and thermal properties of metakaolin-fly ash geopolymers. Sustain. Chem. Pharm. 26:100620. https://doi.org/10.1016/j.scp.2022.100620.
17. Amran M, Fediuk R, Murali G, Avudaiappan S, Ozbakkaloglu T, Vatin N. 2021. Fly ash-based eco-efficient concretes:A comprehensive review of the short-term properties. Materials. 14(15):4264. https://doi.org/10.3390/ma14154264.
18. Li JY, Wang JM. 2019. Comprehensive utilization and environmental risks of coal gangue:A review. J. Clean. Prod. 239:117946. https://doi.org/10.1016/j.jclepro.2019.117946.
19. Peng C, Dai GF, Wang YH, Yang JH, Wang CX. 2024. Preparation of high-strength ceramsite from coal gangue and printing and dyeing sludge:Design strategy and modelling mechanism. Ceram. Int. 50(11, Part B):19963-19970. https://doi.org/10.1016/j.ceramint.2024.03.122.
20. Zhao YF, Zhang YJ, Zhao Q. 2025. Modification of residual sludge biochar and its phosphorus conversion behavior. J. Inner. Mongolia. Univ. Technol. Nat. Sci. Ed. 44(03):202-209. https://doi.org/10.13785/j.cnki.nmggydxxbzrkxb.2025.03.002.
21. Li CB, Zhang GF, Liu DZ, Wang MT. 2023. Preparation of lightweight ceramsite from solid waste lithium slag and fly ash. Constr. Build. Mater. 398:132419. https://doi.org/10.1016/j.conbuildmat.2023.132419.
22. Wang LS, Wang YX, Sun W, Wang CW, Meng XS. 2023. Preparation of lightweight and high-strength ceramsite from highly doped coal fly ash. T. Nonferr. Metal. Soc. 33(12):3885-3898. https://doi.org/10.1016/S1003-6326(23)66378-2.
23. Wan YJ, Wu XY, Zhang HH, Xu YQ, Li CY, Xu YF. 2024. Exploring mechanical properties and long-term environmental impact of ceramsites derived from diverse solid wastes. Waste. Manage. 190:538-547. https://doi.org/10.1016/j.wasman.2024.10.012.
24. Xiao TT, Wang Y, Fan XY, Pan ZQ, Wang HR, Zhou H. 2024. Preparation of eco-friendly and high-strength ceramsite by granite scraps, granite fine mud, and phosphogypsum:Response surface methodology optimization, environmental safety assessment. Process. Saf. Environ. 192:960-972. https://doi.org/10.1016/j.psep.2024.10.085.
25. Wang XX, Qin YH, Okeke I, He C, Li XJ, Wei YX, Yuan J. 2024. Revealing the intrinsic sintering mechanism of high-strength ceramsite from CFB fly ash:Focus on the role of CaO. Ceram. Int. 50(13, Part B):24281-24292. https://doi.org/10.1016/j.ceramint.2024.04.158.

26. Duan X, Huang Y, Li Y, Zhang W, Huang ZW. 2023. Evolution mechanism of pore structure in sintered coal gangue ceramsites. Ceram. Int. 49(19):31385-31395. https://doi.org/10.1016/j.ceramint.2023.07.086.
27. Wang CQ, Duan DY, Huang DM, Chen Q, Tu MJ, Wu K. 2022. Lightweight ceramsite made of recycled waste coal gangue & municipal sludge: Particular heavy metals, physical performance and human health. J. Clean. Prod. 376:134309. https://doi.org/10.1016/j.jclepro.2022.134309.
28. Shao Y, Zhang W. 2022. Preparation of municipal solid waste incineration fly ash-based ceramsite and its mechanisms of heavy metal immobilization. Waste. Manage. 143:54-60. https://doi.org/10.1016/j.wasman.2022.02.021.
29. Han Y, Zhou M, Wang JJ, Tian Y, Wang XY. 2024. Optimization of coal-based solid waste ceramsite foam concrete mix proportions and performance study. Constr. Build. Mater. 416:135226. https://doi.org/10.1016/j.conbuildmat.2024.135226.
30. Wu XG, Wang SR, Yang JH, Zhu S, Kodama J. 2020. Mechanical properties and dynamic constitutive relation of lightweight shale ceramsite concrete. Eur. J. Environ. Civ. En. 26(7):2898-2912. https://doi.org/10.1080/19648189.2020.1782772.
31. Li J, Dong W, Zhao XY, Li H. 2024. Investigation on fracture properties of concrete considering the viscoelastic characteristics. Constr. Build. Mater. 426:136044. https://doi.org/10.1016/j.conbuildmat.2024.136044.
32. Chang ZY, Long GC, Zhou JL, Ma C. 2020. Valorization of sewage sludge in the fabrication of construction and building materials:A review. Resour. Conserv. Recy. 154:104606. https://doi.org/10.1016/j.resconrec.2019.104606.
33. Xie JH, Zhao JB, Wang JJ, Huang PY, Liu JF. 2021. Investigation of the high-temperature resistance of sludge ceramsite concrete with recycled fine aggregates and GGBS and its application in hollow blocks. J. Build. Eng. 34:101954. https://doi.org/10.1016/j.jobe.2020.101954.
34. Xia SX, Lin R, Cui X, Shan J. 2016. The application of orthogonal test method in the parameters optimization of PEMFC under steady working condition. Int. J. Hydrogen. Energy. 41(26):11380-11390. https://doi.org/10.1016/j.ijhydene.2016.04.140.
35. Deng WY, Ma JC, Xiao JM, Wang L, Su YX. 2019. Orthogonal experimental study on hydrothermal treatment of municipal sewage sludge for mechanical dewatering followed by thermal drying. J. Clean. Prod. 209:236-249. https://doi.org/10.1016/j.jclepro.2018.10.261.
36. Jiang B, Xia WJ, Wu T, Liang JH. 2021. The optimum proportion of hygroscopic properties of modified soil composites based on orthogonal test method. J. Clean. Prod. 278:123828. https://doi.org/10.1016/j.jclepro.2020.123828.
37. Zhao Y, Liang NX, Chen H, Li Y. 2020. Preparation and properties of sintering red mud unburned road brick using orthogonal experiments. Constr. Build. Mater. 238:117739. https://doi.org/10.1016/j.conbuildmat.2019.117739.
38. Jiang B, Xia WJ, Wu T, Liang JH. 2021. The optimum proportion of hygroscopic properties of modified soil composites based on orthogonal test method. J. Clean. Prod. 278:123828. https://doi.org/10.1016/j.jclepro.2020.123828.
39. Qian LP, Xu LY, Alrefaei YZ. 2022. Artificial alkali-activated aggregates developed from wastes and by-products:A state-of-the-art review. Resour. Conserv. Recy. 177:105971. https://doi.org/10.1016/j.resconrec.2021.105971.
40. Kockal NU, Ozturan T. 2011. Durability of lightweight concretes with lightweight fly ash aggregates. Constr. Build. Mater. 25(3):1430-1438. https://doi.org/10.1016/j.conbuildmat.2010.09.022.
41. Zhang WP, Min HG, Gu XL, Xi YP, Xing YS. 2015. Mesoscale model for thermal conductivity of concrete. Constr. Build. Mater. 98:8-16. https://doi.org/10.1016/j.conbuildmat.2015.08.106.
42. Guo Y, Liu Y, Wang W, Zhang Y, Wang ZX, Jiang L. 2020. A study on heat transfer performance of recycled aggregate thermal insulation concrete. J. Build. Eng. 32:101797. https://doi.org/10.1016/j.jobe.2020.101797.
43. Vargas P, Baena OR, Tobón JI. 2017. Microstructural analysis of interfacial transition zone (ITZ) and its impact on the compressive strength of lightweight concretes. Constr. Build. Mater. 137:381-389. https://doi.org/10.1016/j.conbuildmat.2017.01.101.
44. Wei LS, Zuo WQ, Pan H, Lyu K, Zhang WH, She W. 2021. Rational design of lightweight cementitious composites with reinforced mechanical property and thermal insulation: Particle packing, hot pressing method, and microstructural mechanisms. Compos. Part B-Eng. 226:109333. https://doi.org/10.1016/j.compositesb.2021.109333.
45. Dai JP, Wang QC, Bi RX, Wang C, Han ZW, Du WT. 2022. Research on influencing factors and time-varying model of thermal conductivity of concrete at early age. Constr. Build. Mater. 315:125638. https://doi.org/10.1016/j.conbuildmat.2021.125638.
46. Hao LC, Xiao JZ, Sun JT, Xia B, Cao WZ. 2022. Thermal conductivity of 3D printed concrete with recycled fine aggregate composite phase change materials. J. Clean. Prod. 364:132598. https://doi.org/10.1016/j.jclepro.2022.132598.
47. Abdellatief M, Ahmed YM, Taman M, Elfadaly E, Tang YC, Abadel AA. 2024. Physico-mechanical, thermal insulation properties, and microstructure of geopolymer foam concrete containing sawdust ash and egg shell. J. Build. Eng. 90:109374. https://doi.org/10.1016/j.jobe.2024.109374.
48. Guo YC, Qian JS, Wang X, Yan ZY, Zhong HD. 2015. Influence of aggregate wettability with different lithology aggregates on concrete drying shrinkage. Adv. Mater. Sci. Eng. 2015:196805. https://doi.org/10.1155/2015/196805.
49. Guo T, Liu Z, Yu C, Ding J, Yu PL, Deng CJ. 2023. Effect of pore structure evolution on mechanical properties and thermal conductivity of porous SiC-Mullite ceramics. Ceram. Int. 49(21):33618-33627. https://doi.org/10.1016/j.ceramint.2023.08.040.
50. Han Y, Li CW, Bian C, Li SB, Wang CA. 2013. Porous anorthite ceramics with ultra-low thermal conductivity. J. Eur. Ceram. Soc. 33(13-14):2573-2578. https://doi.org/10.1016/j.jeurceramsoc.2013.04.006.

51. Nur AJ, Liew YM, Heah CY. 2020. Correlation between pore structure, compressive strength and thermal conductivity of porous metakaolin geopolymer. Constr. Build. Mater. 247:118641. https://doi.org/10.1016/j.conbuildmat.2020.118641.
52. Ding D, Huang R, Wang X, Zhang S, Wu Y, Zhang X. 2022. Thermally conductive silicone rubber composites with vertically oriented carbon fibers: a new perspective on the heat conduction mechanism. Chem. Eng. J. 441:136104. https://doi.org/10.1016/j.cej.2022.136104.
53. Cai SH, Deng XP, Beiyuan JZ, Chen X, Liu DF. 2024. Review of synthetic polymer-based thermal insulation materials in construction and building. J. Build. Eng. 97:110846. https://doi.org/10.1016/j.jobe.2024.110846.
54. Mütevelli Özkan G, Aldemir K, Alhasan O, Benli A, Bayraktar OY. 2024. Investigation on the sustainable use of different sizes of sawdust aggregates in eco-friendly foam concretes: Physico-mechanical, thermal insulation and durability characteristics. Constr. Build. Mater. 438:137100. https://doi.org/10.1016/j.conbuildmat.2024.137100.
55. Shi JY, Zhang MH, Zhu XZ, Yalçınkaya Ç, Çopuroğlu O, Liu YC. 2024. Evaluation of thermal insulation capacity and mechanical performance of a novel low-carbon thermal insulating foam concrete. Energ. Buildings. 323:114744. https://doi.org/10.1016/j.enbuild.2024.114744.
56. Constantinides G, Ulm FJ. 2004. The effect of two types of C-S-H on the elasticity of cement-based materials:Results from nanoindentation and micromechanical modeling. Cem. Concr. Res. 34(1):67-80. https://doi.org/10.1016/S0008-8846(03)00230-8.
57. Liu K, Lu L, Wang F, Liang W. 2017. Theoretical and experimental study on multi-phase model of thermal conductivity for fiber reinforced concrete. Constr. Build. Mater. 148:465-475. https://doi.org/10.1016/j.conbuildmat.2017.05.043.
58. Qomi MJA, Ulm FJ, Pelleng RJM. 2015. Physical origins of thermal properties of cement paste. Phys. Rev. Appl. 3(6):064010. https://doi.org/10.1103/PhysRevApplied.3.064010.
59. Du YB, Ge Y. 2022. Modeling of effective thermal conductivity of cement paste. J. Chin. Ceram. Soc. 50(02):466-472.
60. Bullard JW, Stuyzman PE. 2006. Analysis of CCRL proficiency cements 151 and 152 using the virtual cement and concrete testing laboratory. Cem. Concr. Res. 36(8):1548-1555. https://doi.org/10.1016/j.cemconres.2006.05.024.
61. Watts BE, Tao C, Ferraro CC. 2018. Proficiency analysis of VCCTL results for heat of hydration and mortar cube strength. Constr. Build. Mater. 161:606-617. https://doi.org/10.1016/j.conbuildmat.2017.09.035.
62. Zhao J, Wang AG, Zhang, ZH, Dai JG, Liu KW, Wang YM, Chu YJ, Sun DS. 2024. Hybrid fiber reinforced ultra-high performance coal gangue geopolymer concrete (UHPGC): Mechanical properties, enhancement mechanism, carbon emission and economic analysis. J. Build. Eng. 96:110428. https://doi.org/10.1016/j.jobe.2024.110428.
63. Tang KJ, An HN, Liu CB, Li YD, Jia LJ. 2024. Safety and environmental protection application of high performance solid waste unburned ceramsite and its lightweight high strength concrete. Sustain. Chem. Pharm. 40:101611. https://doi.org/10.1016/j.scp.2024.101611.
64. Wang CQ, Cheng LX, Ying Y, Yang FH. 2024. Utilization of all components of waste concrete: Recycled aggregate strengthening, recycled fine powder activity, composite recycled concrete and life cycle assessment. J. Build. Eng. 82:108255. https://doi.org/10.1016/j.jobe.2023.108255.
65. Li LF, Shao X, Ling TC. 2023. Life cycle assessment of coal gangue composite cements: From sole OPC towards low-carbon quaternary binder. J. Clean. Prod. 414:137674. https://doi.org/10.1016/j.jclepro.2023.137674.
66. Yu J, Lu C, Leung KY, Li GY. 2017. Mechanical properties of green structural concrete with ultrahigh-volume fly ash. Constr. Build. Mater. 147:510-518. https://doi.org/10.1016/j.conbuildmat.2017.04.188.
67. Liu J, Li ZL, Zhang WZ, Jin HS, Xing F, Tang LP. 2022. The impact of cold-bonded artificial lightweight aggregates produced by municipal solid waste incineration bottom ash (MSWIBA) replace natural aggregates on the mechanical, microscopic and environmental properties, durability of sustainable concrete. J. Clean. Prod. 337:130479. https://doi.org/10.1016/j.jclepro.2022.130479.